

ON THE DETERMINATION OF THE MECHANICAL PROPERTIES OF WIND TURBINE BLADES: GEOMETRICAL ASPECTS OF LINE BASED ALGORITHMS

C. Martín Saravia ^{a,b}, Claudio D. Gatti ^a, José M. Ramirez ^a

^a *Grupo de Investigación en Multifísica Aplicada, CONICET – Universidad Tecnológica Nacional, Facultad Regional Bahía Blanca, Bahía Blanca, Argentina.*

^b *Centro de Investigación en Mecánica Teórica y Aplicada, CONICET – Universidad Tecnológica Nacional, Facultad Regional Bahía Blanca, Bahía Blanca, Argentina.*

Abstract. This paper discusses the aspects relating the geometric discretization of anisotropic wind turbine blade cross sections via line elements and the calculation of its mechanical properties. The geometrical reconstruction of the blade is done through an algorithm that reads a table that contains the representation of the aerodynamic profile of the blade as a set of connected line segments. The composite material theoretical background is based on a vector variant of the classical lamination theory embedded into a geometrically exact large deformation-small strain thin-walled beam formulation; transverse shear and out of plane warping effects are considered. The impact of the geometric reconstruction in the accuracy of the mechanical properties is studied using both rectangular and trapezoidal elements. It is found that a proper geometrical reconstruction of the cross section must be ensured to obtain small errors in the mechanical properties. It is shown that line based algorithms can give very accurate results provided the cross section geometry is adequately represented.

Keywords: Wind turbines; Composite materials; Finite elements; thin-walled beams; cross section

* Corresponding Author.

E-mail address: msaravia@conicet.gov.ar (C.M. Saravia)

1 INTRODUCTION

Renewable energy is increasingly contributing to the global energy generation; biomass, wind, solar and geothermal energies, thermoelectricity, etc., are just a few of the many clean sources that are being used nowadays to obtain energy without affecting the environment [1-5]. Among them, wind energy is clearly one the most exploited sources.

Wind turbines are almost exclusively used to extract energy from the wind; its study is of paramount importance for increasing the current global energy production. The performance of a wind turbine is governed mainly by the rotor; its design involves the study of a wide variety of subjects; among them, the blade design is the most important.

Computational modeling of composite wind turbine blades is a hot research subject [3, 6-10]; both 3D, 2D and 1D modeling techniques have been investigated extensively. Most modern approaches make use of finite elements, so the response of the blade is typically computed after some kind of discretization.

In the most general case, the full blade can be discretized into solid finite elements; however, this three dimensional modeling technique is rarely used since the time and computation resources required to generate such a complex geometry are huge. Besides, the aeroelastic

nature of the blade dynamics makes a full fluid-structure 3D simulation using solid elements very difficult to execute. This opens the possibility for a wide variety of the so-called “reduced theories”, which make use of various hypotheses to model the structural behavior of the blade; they simplify the geometrical representation blade and also the description of its mechanical behavior.

Currently, three approaches are predominantly used to simulate the mechanics of composite wind turbine blades:

i) 3D shell approaches, where the outer surface of the blade is discretized into tridimensional surface elements of composite material that deform arbitrarily in space [11]. This approach is often used in serial with a method to extract the cross sectional properties of the blade at a certain span location via static loading [10-13]. The geometrical errors arising from the definition of the cross section as a set of shell elements cannot be avoided; although, the accuracy of the method is generally good [12].

ii) Coupled surface-line algorithms (SLAs), where the blade is conceived as a set of cross sections modeled as 2D continuum elements; the group of cross sections move solidary to a reference 3D curve that deforms in space following the kinematic laws imposed by certain beam theory [14-16]. This is probably the most accurate approach to describe the mechanic behavior of the blade since the cross sectional modeling with 2D elements permits a fine description of the blade geometric constructive details; also, the cross sectional algorithm can be coupled with almost any beam theory.

iii) Coupled line-line algorithms (LLAs), where the blade is conceived as a set of cross sections modeled as 2D line elements; the group of cross sections move solidary to a reference 3D curve that deforms in space following the kinematic laws imposed by certain beam theory [14-16]. The accuracy of the LLAs is dependent on the geometrical reconstruction algorithm and the composite material formulation. The accuracy of modern LLAs is very good; for certain cross sections LLA can give more accurate results than 3D shell approaches [12].

Although SLAs are more accurate than LLAs, the survival of LLAs is favored by the following important factors: i) the high time consumption for the creation and execution of a SLA model, ii) the difficulty of SLAs to handle very small thickness layers of paint and coating and iii) the impossibility to use LLAs coupled with geometrical optimization software without implying the generation of a new mesh and the interaction with a user.

Both LLs and SLAs are structured such that a beam theory is fed with a matrix of cross sectional stiffness coefficients, which are individually obtained a priori. However, in SLAs the coefficients are obtained through finite element modeling of the cross sectional shape with 2D continuum elements.

In LLAs, thin-walled beam theory is used in linear and nonlinear variants [10, 15-18]. Researchers have dedicated thirty years of efforts to formulate thin-walled beam theories; almost every work found in the literature concludes that refinements in the constitutive and kinematic aspects of the formulations lead to significant improvements in the theory. Static displacements, stresses, natural frequencies and frequency response of the beam have been used to test the effects of the proposed theoretical improvements. The impact of the geometric description of the cross section in the accuracy of the thin-walled theory has been addressed very rarely; in this paper this will be shown to be of paramount importance for obtaining accurate results.

Nowadays LLAs are widely used in rotor design to determine the cross sectional stiffness of blades. Chen et. al [15] presented a detailed assessment of computational tools for calculating wind turbine blade cross sectional stiffness. This study includes numerical comparisons between: thin walled beam theory, the SLA VABS (the most renowned algorithm for the determination of cross sectional properties, developed by Prof. Hodges and coworkers [14, 16, 19]) and the LLAs: FAROB [20] (developed at the Dutch Knowledge Center of Wind Energy Materials and Construction), PreComp [21] (developed at National Renewable Energy

Laboratory in USA) and CROSTAB [22] (Cross Sectional Stability of Anisotropic Blades, developed at the Energy Research Center of the Netherlands). The study concludes that the LLAs are inconsistent and therefore its applicability to modeling realistic blades is questionable; the present paper will show that this conclusion is misleading.

Resor et. al [23] compared results obtained with PreComp and BPE (Blade Property Extraction, a 3D shell approach developed by Global Energy Concepts and Sandia National Laboratories [24]), to those obtained in experimental testing of the BSDS blade; according to this paper the overall difference between PreComp and BPE is in the range of 15-25% and the difference between the experimental results and BPE are in the range of 5-20%. In a later study, Resor and Paquette also included VABS in the assessment of cross sectional stiffness calculations [25]. The paper reproduced the same results of [15] for a particular wind turbine cross section, only the diagonal terms of the stiffness matrix were presented. For the CX-100 blade, discrepancies were found between VABS and BPE, especially in sections near the blade's root. These discrepancies were attributed to local straining.

In a previous work, the authors have presented LL formulation to obtain the cross sectional properties of composite cross sections; the work showed that a LLA can be very accurate provided it is correctly implemented [12]. In the present paper, an improved version of the previously presented LLA is used to analyze the impact of the discretization aspects on the accuracy of the results. The composite material theoretical background is based on a vector variant of the classical lamination theory embedded into a geometrically exact large deformation-small strain thin-walled beam formulation; transverse shear and out of plane warping effects are considered. The geometrical reconstruction of the cross section is performed with two types of segments: classical thin-walled beam theory rectangular segments and a variable layer length trapezoidal segments. The influence of the number of layers in the laminate also studied. It is shown that the choice of the reconstruction technique greatly affects the prediction of the cross sectional parameters. The 1D nature of the approach permits its use in optimization studies, when variation of parameters must be executed without requiring user interaction. The approach gives excellent results with minimal modeling time; results are often better than 3D approaches.

2 THEORETICAL ASPECTS

2.1 Beam Formulation

The cross sectional parameters are dependent on the beam formulation; they are uniquely defined for a particular strain energy function. As a consequence, a particular cross sectional stiffness measure is strictly consistent only with the kinematic formulation from which it was derived. A detailed derivation of the composite beam formulation used in this paper can be found in [12, 26]; hereafter, only relevant details are reproduced.

It is assumed that the blade is moderately slender; so its mechanic behavior can be reasonably approximated by beam theory.

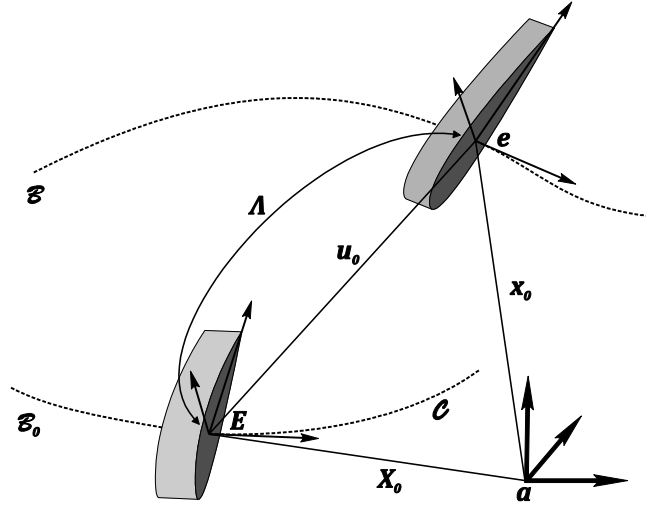


Figure 1- Wind turbine blade finite kinematic description.

The position vectors of a point in the blade in the undeformed and deformed configuration can respectively be expressed as [12]:

$$\begin{aligned} \mathbf{X}(x, \xi_2, \xi_3) &= \mathbf{X}_0(x) + \sum_{i=2}^3 \xi_i \mathbf{E}_i, \\ \mathbf{x}(x, \xi_2, \xi_3, t) &= \mathbf{x}_0(x, t) + \sum_{i=2}^3 \xi_i \mathbf{e}_i + \omega \mathbf{e}_1. \end{aligned} \quad (1)$$

In both above equations \mathbf{X}_0 is the position of the pole in the reference configuration, \mathbf{x}_0 is the position of the pole in the deformed configuration and the coordinates ξ_2 and ξ_3 are the components of the position vector of a point in the cross section in \mathbf{E}_i , see Figure 1. The variable ω accounts for the displacements in the cross section due to torsional warping.

Three frames of reference attached to the cross section are introduced: a) a reference material frame $\{\mathbf{E}_1, \mathbf{E}_2, \mathbf{E}_3\}$, b) a sectional frame $\{\mathbf{E}_1, \hat{\mathbf{n}}, \hat{\mathbf{s}}\}$ and c) a layer individual frame $\{\hat{\mathbf{1}}, \hat{\mathbf{2}}, \hat{\mathbf{3}}\}$, see Figure 2.

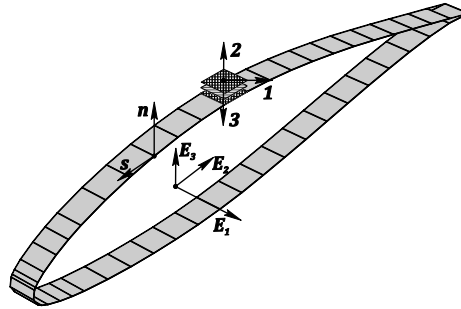


Figure 2- Blade local reference systems.

The Green-Lagrange strain tensor is defined as a function of the deformation gradient \mathbf{F} as

$$\mathbf{E} = \frac{1}{2}(\mathbf{F}^T \mathbf{F} - \mathbf{I}); \quad (2)$$

this expression can measure arbitrary straining. It can be shown that the deformation gradient has the following expression [12]

$$\mathbf{F} = \mathbf{\Lambda} + (\mathbf{x}'_0 - \mathbf{e}_1 + \xi_\alpha \mathbf{e}'_\alpha) \otimes \mathbf{E}_1, \quad (3)$$

where $\mathbf{\Lambda}$ is the finite rotation tensor of the cross section. The GL strain tensor is then

$$\mathbf{E} = \frac{1}{2} \begin{bmatrix} 2\boldsymbol{\epsilon} \cdot \mathbf{e}_1 & \boldsymbol{\epsilon} \cdot \mathbf{e}_2 & \boldsymbol{\epsilon} \cdot \mathbf{e}_3 \\ \boldsymbol{\epsilon} \cdot \mathbf{e}_2 & 0 & 0 \\ \boldsymbol{\epsilon} \cdot \mathbf{e}_3 & 0 & 0 \end{bmatrix}. \quad (4)$$

155 where

$$\boldsymbol{\epsilon} = \mathbf{x}'_0 - \mathbf{e}_1 + \xi_\alpha \mathbf{e}'_\alpha, \quad (5)$$

156 The Small Green Strain Tensor (SGS) can now be written in vector form as [12]

$$\mathbf{e} = \begin{bmatrix} \mathbf{x}'_0 \cdot \mathbf{e}_1 - 1 + \xi_\alpha \mathbf{e}'_\alpha \cdot \mathbf{e}_1 \\ \mathbf{x}'_0 \cdot \mathbf{e}_2 + \xi_3 \mathbf{e}'_3 \cdot \mathbf{e}_2 \\ \mathbf{x}'_0 \cdot \mathbf{e}_3 + \xi_2 \mathbf{e}'_2 \cdot \mathbf{e}_3 \end{bmatrix}. \quad (6)$$

157 The SGS tensor can be split into a geometrical part and a generalized strain part

$$\mathbf{e} = \mathbf{D}\boldsymbol{\varepsilon}, \quad (7)$$

158 being \mathbf{D} a cross sectional matrix such that

$$\mathbf{D} = \begin{bmatrix} \mathbf{E}_1 & \mathbf{r} \\ \mathbf{E}_2 & \mathbf{r} \times \mathbf{E}_2 \\ \mathbf{E}_3 & \mathbf{r} \times \mathbf{E}_3 \end{bmatrix}, \quad (8)$$

159 and $\boldsymbol{\varepsilon}$ the generalized strain vector.

$$\boldsymbol{\varepsilon} = \begin{bmatrix} \mathbf{x}'_0 \cdot \mathbf{e}_1 - 1 \\ \mathbf{x}'_0 \cdot \mathbf{e}_2 \\ \mathbf{x}'_0 \cdot \mathbf{e}_3 \\ \mathbf{e}'_2 \cdot \mathbf{e}_3 \\ \mathbf{e}'_2 \cdot \mathbf{e}_1 \\ \mathbf{e}'_3 \cdot \mathbf{e}_1 \end{bmatrix}. \quad (9)$$

160 For simplicity and without implying a simplification it has been assumed that $\mathbf{E}_i = \mathbf{a}_i$.

161 Lastly, the curvature and axial-shear strain vectors are defined for future use as

$$\boldsymbol{\gamma} = [\epsilon \quad \gamma_2 \quad \gamma_3]^T = [\mathbf{x}'_0 \cdot \mathbf{e}_1 - 1 \quad \mathbf{x}'_0 \cdot \mathbf{e}_2 \quad \mathbf{x}'_0 \cdot \mathbf{e}_3]^T, \quad (10)$$

$$\boldsymbol{\kappa} = [\kappa_1 \quad \kappa_2 \quad \kappa_3]^T = [\mathbf{e}'_2 \cdot \mathbf{e}_3 \quad \mathbf{e}'_2 \cdot \mathbf{e}_1 \quad \mathbf{e}'_3 \cdot \mathbf{e}_1]^T.$$

162 Then the generalized strain vector can be written in the form

$$\boldsymbol{\varepsilon} = [\boldsymbol{\gamma}^T \quad \boldsymbol{\kappa}^T]^T. \quad (11)$$

163 2.2 The sectional strain measures

164 The SGS vector expresses the strain state of the blade in the reference frame. In order to
165 write the constitutive equations together with the cross sectional hypotheses it is necessary
166 to express the SGS in the cross sectional frame $\{\mathbf{E}_1, \hat{\mathbf{n}}, \hat{\mathbf{s}}\}$.

167 Recall that the origin of the cross sectional system moves along the cross section contour
168 (placed half a thickness inward from the outer contour) in anticlockwise direction; then the
169 tangent unit vector can be found as the derivative of the mid-contour position vector $\bar{\mathbf{r}} =$
170 $\bar{\xi}_2 \mathbf{E}_2 + \bar{\xi}_3 \mathbf{E}_3$. This is

$$\hat{\mathbf{s}} = \frac{d\bar{\mathbf{r}}}{ds} = \bar{\xi}'_2 \mathbf{E}_2 + \bar{\xi}'_3 \mathbf{E}_3, \quad (12)$$

171 where $\bar{\xi}'_i$ represents derivatives of mid-contour cross sectional coordinates with respect to
 172 s . The normal unit vector can be obtained invoking the orthogonality condition of the
 173 coordinate system

$$\hat{\mathbf{n}} = \hat{\mathbf{s}} \times \mathbf{E}_1 = \bar{\xi}'_3 \mathbf{E}_2 - \bar{\xi}'_2 \mathbf{E}_3. \quad (13)$$

174 Then the position vector of a point in the cross section expressed in the sectional coordinate
 175 system is

$$\begin{aligned} \mathbf{r}_s &= (\bar{r}_n + n)\hat{\mathbf{n}} + \bar{r}_s \hat{\mathbf{s}}, \\ \bar{\mathbf{r}}_s &= \bar{r}_n \hat{\mathbf{n}} + \bar{r}_s \hat{\mathbf{s}}, \end{aligned} \quad (14)$$

176 where the mid-contour components are obtained as

$$\begin{aligned} \bar{r}_n &= \bar{\mathbf{r}}_s \cdot \hat{\mathbf{n}} = \bar{\xi}_2 \bar{\xi}'_3 - \bar{\xi}_3 \bar{\xi}'_2, \\ \bar{r}_s &= \bar{\mathbf{r}}_s \cdot \hat{\mathbf{s}} = \bar{\xi}_2 \bar{\xi}'_2 + \bar{\xi}_3 \bar{\xi}'_3. \end{aligned} \quad (15)$$

177 Another needed relation is the position of a point in the cross section as a function of the
 178 mid-contour coordinates, this is

$$\mathbf{r} = \bar{\mathbf{r}} + n\hat{\mathbf{n}} = (\bar{\xi}_2 + n\bar{\xi}'_3)\mathbf{E}_2 + (\bar{\xi}_3 - n\bar{\xi}'_2)\mathbf{E}_3. \quad (16)$$

179 Now, a sectional frame transformation tensor \mathbf{Q}_s is introduced (see [12]). \mathbf{Q}_s operates over
 180 the SGS tensor to give the strains in the sectional system as

$$\mathbf{e} = \mathbf{Q}_s^T \mathbf{E} \mathbf{Q}_s; \quad (17)$$

181 Thus, the vector form of the sectional strain is

$$\mathbf{e} = \begin{bmatrix} \epsilon_x \\ \gamma_{xs} \\ \gamma_{xn} \end{bmatrix} = \begin{bmatrix} \epsilon + \bar{\xi}_2 \kappa_2 + \bar{\xi}_3 \kappa_3 \\ \bar{\xi}'_2 \gamma_2 + \bar{\xi}'_3 \gamma_3 + (\bar{\xi}_2 \bar{\xi}'_3 - \bar{\xi}_3 \bar{\xi}'_2) \kappa_1 \\ \bar{\xi}'_3 \gamma_2 - \bar{\xi}'_2 \gamma_3 - (\bar{\xi}_2 \bar{\xi}'_2 + \bar{\xi}_3 \bar{\xi}'_3) \kappa_1 \end{bmatrix}; \quad (18)$$

182 From the above expression, expansion of the terms $\bar{\xi}_i$ gives

$$\mathbf{e} = \begin{bmatrix} \epsilon + (\bar{\xi}_2 + n\bar{\xi}'_3) \kappa_2 + (\bar{\xi}_3 - n\bar{\xi}'_2) \kappa_3 \\ \bar{\xi}'_2 \gamma_2 + \bar{\xi}'_3 \gamma_3 + ((\bar{\xi}_2 + n\bar{\xi}'_3) \bar{\xi}'_3 - (\bar{\xi}_3 - n\bar{\xi}'_2) \bar{\xi}'_2) \kappa_1 \\ \bar{\xi}'_3 \gamma_2 - \bar{\xi}'_2 \gamma_3 - ((\bar{\xi}_2 + n\bar{\xi}'_3) \bar{\xi}'_2 + (\bar{\xi}_3 - n\bar{\xi}'_2) \bar{\xi}'_3) \kappa_1 \end{bmatrix}. \quad (19)$$

183 Now, arranging some terms in the last equation and using Eqs. (15) the following compact
 184 expression for the sectional SGS is found

$$\mathbf{e}_s = \begin{bmatrix} \epsilon_x \\ \gamma_{xs} \\ \gamma_{xn} \end{bmatrix} = \begin{bmatrix} \epsilon + (\kappa_3 \bar{\xi}_2 + \kappa_2 \bar{\xi}_3) + n(\kappa_3 \bar{\xi}'_3 - \kappa_2 \bar{\xi}'_2) \\ (\bar{\xi}'_2 \gamma_2 + \bar{\xi}'_3 \gamma_3) + \kappa_1 \bar{r}_n \\ (\bar{\xi}'_3 \gamma_2 - \bar{\xi}'_2 \gamma_3) - \kappa_1 \bar{r}_s \end{bmatrix}, \quad (20)$$

185 Finally, the last equation can be written as a function of the generalized strains as

$$\mathbf{e}_s = \mathbf{D}_s \boldsymbol{\varepsilon} = \begin{bmatrix} \mathbf{1} & \mathbf{r} \\ \hat{\mathbf{s}} & r_n \mathbf{1} \\ \hat{\mathbf{n}} & -\bar{r}_s \mathbf{1} \end{bmatrix} \begin{bmatrix} \boldsymbol{\gamma} \\ \boldsymbol{\kappa} \end{bmatrix} \quad (21)$$

where $r_n = \bar{r}_n + n$.

3 COMPOSITE MATERIAL MODELING

3.1 Constitutive relations

A wide variety of formulations can be derived from the different hypotheses that can be made about the constitutive behavior of the cross. It was shown in [12] that even the simplest constitutive formulation can give accurate results for most cross sections.

Following [12], the layer frame of reference $\{\hat{\mathbf{1}}, \hat{\mathbf{2}}, \hat{\mathbf{3}}\}$ will be used to derive the constitutive equations; it will serve to describe locally the mechanical behavior of the layer. Every layer of composite material is assumed to lie in the $\{\mathbf{E}_1, \hat{\mathbf{s}}\}$ plane and thus the normal direction $\hat{\mathbf{n}}$ of the sectional frame is coincident with $\hat{\mathbf{2}}$ in the layer frame.

Assuming orthotropic layers the constitutive equations are written as

$$\begin{bmatrix} \sigma_1 \\ \sigma_2 \\ \sigma_3 \\ \sigma_{23} \\ \sigma_{31} \\ \sigma_{12} \end{bmatrix} = \begin{bmatrix} C_{11} & C_{12} & C_{13} & 0 & 0 & 0 \\ C_{12} & C_{22} & C_{23} & 0 & 0 & 0 \\ C_{13} & C_{23} & C_{33} & 0 & 0 & 0 \\ 0 & 0 & 0 & C_{44} & 0 & 0 \\ 0 & 0 & 0 & 0 & C_{55} & 0 \\ 0 & 0 & 0 & 0 & 0 & C_{66} \end{bmatrix} \begin{bmatrix} \epsilon_1 \\ \epsilon_2 \\ \epsilon_3 \\ \gamma_{23} \\ \gamma_{31} \\ \gamma_{12} \end{bmatrix}, \quad (22)$$

where σ_i and ϵ_i are the layer stress and strains and C_{ij} are the layer stiffness coefficients [12].

It must be noted that the orthotropicity assumption at the layer level does not imply that the laminate is also orthotropic; orthotropic layers can be stacked in arbitrary angle sequences to give a generally anisotropic laminate. Although the layer orthotropicity assumption does not generate a significant simplification to the theory and certainly could be avoided, most materials used in wind turbine blade design are locally orthotropic and thus it is convenient to retain it to ease the computational implementation.

Invoking the constraints imposed by the kinematic hypotheses in section would require to set $\epsilon_2 = \gamma_{23} = \gamma_{12} = 0$. To avoid the over stiffening of the beam it is chosen to set $\sigma_2 = \sigma_{23} = \sigma_{12} = 0$, which gives the flexibility equation

$$\begin{bmatrix} \epsilon_1 \\ \epsilon_3 \\ \gamma_{13} \end{bmatrix} = \begin{bmatrix} S_{11} & S_{13} & 0 \\ S_{13} & S_{33} & 0 \\ 0 & 0 & S_{55} \end{bmatrix} \begin{bmatrix} \sigma_1 \\ \sigma_3 \\ \sigma_{13} \end{bmatrix} \quad (23)$$

being S_{11} the stiffness coefficients.

The last expression is now transformed to the sectional frame to obtain the following compliance equations

$$\begin{bmatrix} \epsilon_x \\ \epsilon_s \\ \gamma_{xs} \end{bmatrix} = \begin{bmatrix} Q_{11} & Q_{12} & Q_{13} \\ & Q_{22} & Q_{23} \\ & & Q_{33} \end{bmatrix} \begin{bmatrix} \sigma_x \\ \sigma_s \\ \tau_{xs} \end{bmatrix} \quad (24)$$

where ϵ_i and σ_i are the strains and stresses in the sectional frame and Q_{ij} are the transformed stiffness coefficients.

By hypothesis of the beam cross section, it is possible to set $\epsilon_s = 0$, then the compliance equations could be corrected accordingly, but it is well known that for composite beams the

214 assumption $\epsilon_s = 0$ leads to a significant overstiffening [18, 27, 28]. Therefore, it convenient to
 215 use the mildly inconsistent hypothesis $\sigma_s = 0$, thus reaching the following constitutive equation

$$\begin{bmatrix} \epsilon_x \\ \gamma_{xs} \end{bmatrix} = \begin{bmatrix} Q_{11} & Q_{13} \\ Q_{13} & Q_{33} \end{bmatrix} \begin{bmatrix} \sigma_x \\ \tau_{xs} \end{bmatrix} \quad (25)$$

216 Inversion gives

$$\begin{bmatrix} \sigma_x \\ \tau_{xs} \end{bmatrix} = \begin{bmatrix} A_{11} & A_{13} \\ A_{13} & A_{33} \end{bmatrix} \begin{bmatrix} \epsilon_x \\ \gamma_{xs} \end{bmatrix} \quad (26)$$

217 Recalling Eq. (21) the constitutive equations can be expressed in matrix form as

$$\boldsymbol{\sigma}_s = \mathbf{C} \mathbf{D}_s \boldsymbol{\epsilon} \quad (27)$$

218 where

$$\boldsymbol{\sigma} = \begin{bmatrix} \sigma_x \\ \tau_{xs} \end{bmatrix}, \quad \mathbf{C} = \begin{bmatrix} A_{11} & A_{13} \\ A_{13} & A_{33} \end{bmatrix}, \quad \mathbf{D}_s = \begin{bmatrix} \mathbf{1} & \mathbf{r} \\ \hat{\mathbf{s}} & r_n \mathbf{1} \end{bmatrix} \quad (28)$$

219 The expression (27) is the constitutive equation that will be used for the calculation of the
 220 cross sectional properties of the composite blade. It must be noted that this expression could
 221 be considered equivalent to the uniaxial stress assumption.

222 3.2 Virtual work principle

223 The derivation of the blade cross sectional stiffness requires the definition of the virtual
 224 work of the elastic forces; the tridimensional version of the virtual work of the internal forces
 225 is given by

$$\delta W_i = \int_V \delta \mathbf{e}^T \boldsymbol{\sigma} dV. \quad (29)$$

226 Recalling Eqs. (27) the internal virtual work of the composite blade is expanded as

$$\begin{aligned} \delta W_i &= \int_V \delta (\mathbf{D}_s \boldsymbol{\epsilon})^T \mathbf{C} \mathbf{D}_s \boldsymbol{\epsilon} dV \\ &= \int_V \delta \boldsymbol{\epsilon}^T \mathbf{D}_s^T \mathbf{C} \mathbf{D}_s \boldsymbol{\epsilon} dV \end{aligned} \quad (30)$$

227 Since the generalized strain vector is only a function of the running length coordinate of the
 228 blade, i.e. x the above equation can be recast in the following form

$$\delta W_i = \int_L \delta \boldsymbol{\epsilon}^T \left(\int_A \mathbf{D}_s^T \mathbf{C} \mathbf{D}_s dA \right) \boldsymbol{\epsilon} dx. \quad (31)$$

229 From the above equation, the term in parentheses is the cross sectional stiffness of the blade

$$\mathbb{D} = \int_A \mathbf{D}_s^T \mathbf{C} \mathbf{D}_s dA. \quad (32)$$

230 Explicitly

$$\mathbb{D} = \int_A \begin{bmatrix} \mathbf{1}^T & \hat{\mathbf{s}}^T \\ \mathbf{r}^T & r_n^\omega \mathbf{1}^T \end{bmatrix} \begin{bmatrix} A_{11} & A_{13} \\ A_{13} & A_{33} \end{bmatrix} \begin{bmatrix} \mathbf{1} & \mathbf{r} \\ \hat{\mathbf{s}} & r_n^\omega \mathbf{1} \end{bmatrix} dA. \quad (33)$$

231 where $r_n^\omega = r_n + \omega'_s$.

232 3.3 Mass and Inertia Tensors

233 For the present formulation the mass and inertia tensors are given by [12]

$$\mathbb{M} = \int_s \int_n \rho \, dn \, ds, \quad \mathbb{J} = \int_s \int_n \tilde{\mathbf{r}}^T \tilde{\mathbf{r}} \, dn \, ds \quad (34)$$

234 The computation of the mass tensor is straightforward since the density is layerwise
 235 constant. This is also the case of the inertia tensor; although, it admits computation in either
 236 the sectional or the global frames. Computation in the sectional frame is often simpler so it is
 237 the approach followed in the present paper. So, the inertia tensor is obtained through

$$\mathbb{J}_s = \int_s \int_n \tilde{\mathbf{r}}^T \tilde{\mathbf{r}} \, dn \, ds = \int_s \int_n \begin{bmatrix} r_n^2 + r_s^2 & 0 & 0 \\ r_s^2 & -r_n r_s & \\ & r_n^2 & \end{bmatrix} dn \, ds \quad (35)$$

238 where $\tilde{\mathbf{r}}$ is the skew symmetric matrix of the position vector \mathbf{r} .

239 Lastly, the transformation to the global frame is done through the sectional transformation
 240 tensor as

$$\mathbb{J} = \mathbf{Q}_s^T \mathbb{J}_s \mathbf{Q}_s. \quad (36)$$

241 4 BLADE GEOMETRICAL MODELING

242 From the structural point of view, the blade is built with two kinds of materials: the ones
 243 which contribute with mass, the ones which contribute with both mass and stiffness. The
 244 former includes coating, painting and filling materials; filling materials have very low stiffness
 245 and are mainly used to increase the local buckling stiffness at specific locations. The latter
 246 includes composites, fabrics, etc.

247 In the computational implementation of the theory the materials not contributing to stiffness
 248 do not pass through the stiffness algorithm. This is convenient not only because the stiffness
 249 matrix computation is faster but also because the problems arising from poor local vector
 250 conditioning due to the extremely small thicknesses of paint and coating are avoided.

251 Commonly, filling materials such as foam or balsa are used in a sandwich-like configuration.
 252 This improves the local stiffness of the laminate at the expense of a minor decrease in the global
 253 stiffness and a major increase in thickness. The latter often renders the cross section thick-
 254 walled; this have two consequences: i) the normal stresses in the thick-walled segment are not
 255 necessarily small and ii) the layers of the laminate are shorter than the outer layers.

256 Since the stiffness of the core material is low, the normal forces transferred through its
 257 thickness can be assumed to be small, then point i) can be disregarded. The consequence in ii)
 258 will be addressed in the following subsections.

259 Note that the assumptions of the present theory are:

- 260 a) *the cross section can undergo finite displacements and finite rotations.*
- 261 b) *the cross section behaves as rigid in its own plane.*
- 262 c) *the cross section is free to warp out of its planes.*
- 263 d) *the warping elastic energy is small.*
- 264 e) *the normal stresses in the plane of the cross sections are negligible.*
- 265 f) *all strains are small.*

266 4.1 Discretization and segment reconstruction

267 In the design of a wind turbine cross sectional shape, the outer contour is fixed by
 268 aerodynamic requirements as a set of points in the two dimensional space. This aerodynamic

profile is converted to lines and then imported into a meshing software to generate a set of two dimensional line segments.

A LLA takes as input the line-discretized aerodynamic profile of the blade and the shear web locations together with a material mapping table. The material table contains the definition of the material constants, the lamination sequences and the thickness distribution.

In order to reconstruct the actual blade geometry, after the discretization process, each segment must be projected inwards in the direction of the surface normal. To perform this operation several possibilities can be devised; in this paper, reconstruction with rectangles and trapezoids will be studied. Surprisingly, the impact of this choice in the accuracy of the thin-walled theory has not been addressed before; this will be shown to be of key importance for obtaining accurate results.

As already said, the outer contour of the cross section is given a priori by the aerodynamic design of the blade. From the geometric point of view, it is relevant the fact that the inner layers of a laminate segment are shorter than the outer layers. This may result trivial, but this point is rarely considered in thin-walled beam theory. Of course, the effect of the curvature variation disappears as the thickness of the laminate tends to zero; but as stated, at various locations of the cross section the wall is very thick due to attend the local buckling strength requirements.

The reconstruction of the blade geometry must be done via projection of the inward normal of the outer contour according to the information given in the lamination table. This opens the possibility for a reconstruction with three segment types: i) unmatching rectangles, ii) matching trapezoids and iii) unmatching trapezoids; see Figure 3.

Unmatching rectangles are constructed through normal projection in the direction of the segment normal; matching trapezoids are constructed using the intersection point of the inner layers, thus avoiding thickness discontinuity; finally, unmatching trapezoids are obtained through projection in the direction of the average nodal normal.

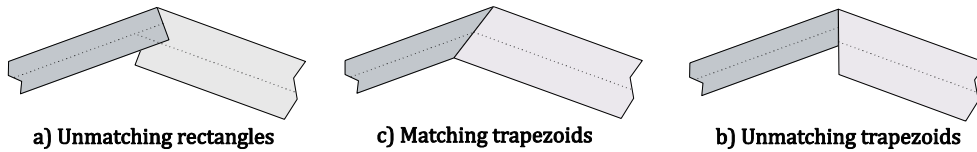


Figure 3 - LLA segment types

There are two important observations that can be made from the visual inspection of Figure 3. Firstly, option a) should overestimate the cross section properties; this is a fact since the reconstruction clearly duplicate the intersection area. Secondly, option b) should give the most accurate representation of an actual thickness transition; although it would be dependent on the local geometric details of the joint between the segments, which cannot be universally defined. This is one of the drawbacks that makes the matching trapezoid not suitable for the geometric reconstruction of unmatching thickness joints; the next paragraphs clarify this.

Firstly, the geometrical aspects of a joint constructed with matching trapezoids are analyzed. Although it may seem trivial to construct a matching trapezoidal joint from the one dimensional mesh of segments, it takes some effort to derive the location of the intersection point of the inner contours of two contiguous segments. Figure 4 shows a typical case where the mid-contours of elements 1 and 2 meet at an undetermined point p .

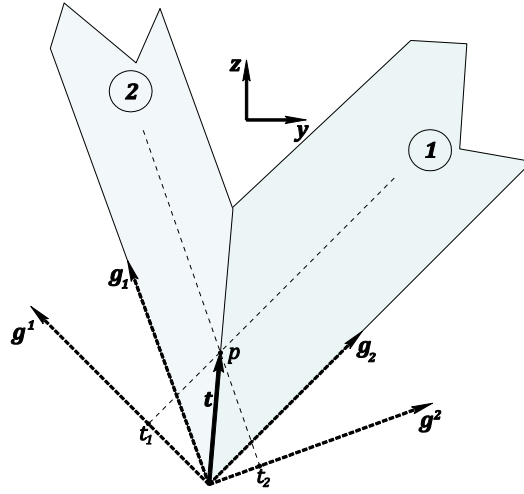


Figure 4 – Non-orthogonal description of the matching trapezoid joint

The unknown is the vector \mathbf{t} , which locates the mid-contours intersection point. Surprisingly, there is no simple vectorial expression to obtain \mathbf{t} ; therefore, posing the problem in non-orthogonal coordinates cannot be avoided. The relative location of the intersection of the mid-contours can be found as

$$\mathbf{t} = t_1 \mathbf{g}^1 + t_2 \mathbf{g}^2, \quad (37)$$

where \mathbf{g}^i is a non-orthogonal basis with unit vectors that are defined from the segment perpendicular vectors. Then, t_i are the covariant components of \mathbf{t} in the base \mathbf{g}^i . The definition of a reciprocal basis such that $\mathbf{g}_i \cdot \mathbf{g}^j = \delta_i^j$ allows to write the covariant components as [29]

$$t_i = \bar{\mathbf{t}} \cdot \mathbf{g}_i. \quad (38)$$

where $\bar{\mathbf{t}}$ is the Cartesian expression of \mathbf{t} , i.e. $\bar{\mathbf{t}} = (c_1 \mathbf{j} + c_2 \mathbf{k})$. Then it is possible to obtain

$$t_i = (c_1 \mathbf{j} + c_2 \mathbf{k}) \cdot \mathbf{g}_i, \quad (39)$$

which gives the following algebraic equation

$$\begin{bmatrix} t_1 \\ t_2 \end{bmatrix} = \begin{bmatrix} \mathbf{j} \cdot \mathbf{g}_1 & \mathbf{k} \cdot \mathbf{g}_1 \\ \mathbf{j} \cdot \mathbf{g}_2 & \mathbf{k} \cdot \mathbf{g}_2 \end{bmatrix} \begin{bmatrix} c_1 \\ c_2 \end{bmatrix}. \quad (40)$$

This can be written as

$$t_i = \mathcal{M}^{ij} c_j, \quad (41)$$

and finally find the Cartesian components of \mathbf{t} as

$$c_i = \mathcal{M}^{ji} t_j. \quad (42)$$

Once the coefficients are determined, both the inner and mid-contour intersections are easily calculated.

However, \mathcal{M}^{ij} is singular when \mathbf{g}_1 and \mathbf{g}_2 are linear combination of each other. Geometrically, this is equivalent to both segments being collinear (or almost collinear); a very common situation for most aerodynamic discrete profiles. In this case, there will no solution for c_i , and thus the algorithmic version of the above formulation will crash.

If the two segments have the same thickness, the situation can be saved since the calculation of the vector can be bypassed through the simple formula

$$\bar{\mathbf{t}} = -\frac{1}{2}e \cdot \check{\mathbf{n}}, \quad (43)$$

where e is the thickness of the laminate and $\check{\mathbf{n}}$ is the outward normal.

On the contrary, if the thicknesses of the parallel elements are not equal, then there is no way to find c_i , then the mid-point cannot be determined. This situation is depicted in Figure 5, where clearly at locations A and B the matching trapezoid formulation would fail to give a joint intersection point.

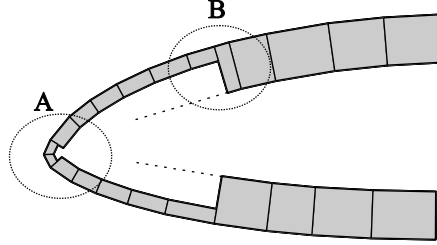


Figure 5 – Discontinuous joint geometry.

In consequence, although a joint that avoid thickness discontinuity may seem attractive at first sight, it is not always a good alternative to represent the laminate transitions. Note that this is not only because the intersection point between the neighbor segments cannot exist, but also because although it exists, it is no guaranteed that the represented joint is similar to the real one. In virtue of the above comments, it is concluded that the matching trapezoid is not a good choice to reconstruct blade cross sections with large thickness changes.

The last conclusion leaves two alternatives for the reconstruction of the sectional geometry, the unmatching rectangles and the unmatching trapezoids. The next sections show how this two types of discretization perform.

4.2 Shear webs and trailing edge reconstruction

The geometric reconstruction of the shear webs and the trailing edge is crucial. Since the shear webs stiffness is very large and the trailing edge is away from the section centroid, the error in the stiffness is likely to be large if the reconstruction is not accurate.

The shear webs are not part of the airfoil profile, so they must be added to the mesh of segments. Shear web segments can be defined by the midline, the left edge or the right edge; any definition is valid as long as the resulting segment is exactly coincident in dimension and location with the actual web.

Algorithmically, the simplest way to reconstruct the shear web is to leave the web segments unconnected with the upper and lower camber segments; thus, defining a convenient offset from the outer contour, the shear web can be reconstructed, see Figure 6.

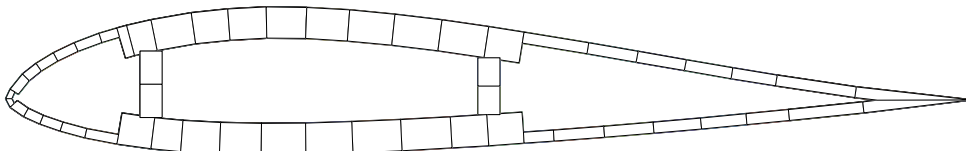


Figure 6 – Reconstructed wind turbine blade

Note that the reconstruction of the trailing edge with unmatching trapezoids requires that the trailing edge joint elements to be long enough to allow the existence the inner contours intersection point without causing annihilation of the quadrilateral segments.

5 NUMERICAL TESTS

This section presents the performance of the formulation in several benchmark tests. They were carefully designed by researchers to compare the modeling capabilities of cross sectional stiffness calculation codes [15]. The presented formulation was implemented computationally in a Python code called CXS.

All comparisons are made assuming that the results obtained with the SLA VABS [14] are the baseline; this is justified by the fact that both its formulation and implementation have been extensively proven [14-16]. For the sake of brevity, in the following examples only the relevant geometric and material data of each example are presented, the reader can refer to [15] for further details. In some examples, results obtained with the LLA PreComp are presented; PreComp was chosen to compare the present formulation mainly because it is the most used LLA [12, 15].

5.1 Thick-walled isotropic tube

The first example is set to test the performance of the algorithm to handle thick segments; an isotropic circular aluminum tube with a thickness to diameter ratio of 1/3 is chosen. VABS and PreComp results are used to benchmark the present algorithm.

The results are presented in Table 1; they show an excellent agreement between VABS and the CXS trapezoidal element; both the stiffness and mass coefficients agree with an error less than 1%.

To increase the accuracy of CXS a layering scheme can be used; this can be easily done in the input file by adding more layers of material in the thickness direction (maintaining the total thickness of the wall). Normally this is of importance when the thickness of the wall is large, a convergence analysis can be executed to determine the optimum number of layers.

| | VABS | PreComp [15] | CXS Trapezoids 10 layers | CXS Trapezoids 5 layers | CXS Rectangles 10 layers |
|---------|------------------------|------------------------|-----------------------------|----------------------------|-----------------------------|
| Axial | 1.834×10^{10} | 2.750×10^{10} | 1.834×10^{10} | 1.834×10^{10} | 2.751×10^{10} |
| Bending | 4.587×10^8 | 5.936×10^8 | 4.575×10^8 | 4.556×10^8 | 5.958×10^8 |
| Torsion | 3.449×10^8 | 4.115×10^8 | 3.439×10^8 | 3.424×10^8 | 4.476×10^8 |
| Mass | 7.037×10^2 | 1.055×10^3 | 7.034×10^2 | 7.034×10^2 | 1.055×10^3 |
| I1 | 3.519×10^1 | - | 3.509×10^1 | 3.495×10^1 | 4.570×10^1 |
| I2 - I3 | 1.759×10^1 | 2.280×10^1 | 1.755×10^1 | 1.747×10^1 | 2.285×10^1 |

Table 1– Thick-walled tube cross sectional properties.

There are some important conclusions that can be drawn from this experiment; i) the trapezoidal segment can reconstruct very effectively the geometry, ii) layering do not improve significantly the accuracy, iii) the rectangular element do not predict well neither of the cross sectional parameters, iv) the PreComp results agree exactly with those of the CXS rectangles. The latter suggests that PreComp errors are very likely due to inaccurate geometry reconstruction.

In virtue of the above, it must be strongly remarked that for the problem at hand the source of error of the LLAs is purely geometric; when the geometry is modeled correctly, as done by CXS trapezoids, the errors tend to zero. The CXS geometric reconstruction with trapezoidal elements of the thick-walled tube can be seen in Figure 7.

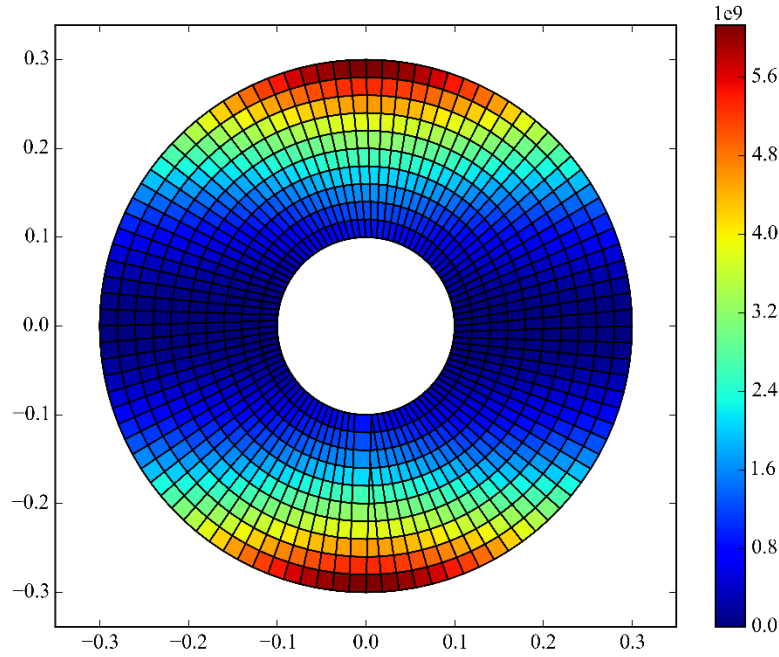


Figure 7 – Bending stiffness density colormap of the thick-walled tube.

5.2 Isotropic blade-like section

In the previous example the material was isotropic and the cross section was bisymmetric, then no stiffness or mass coupling terms appear in the stiffness matrix. In order to test the influence of the geometrical coupling a monosymmetric isotropic section proposed by Chen et al. [15] is studied.

| | VABS | PreComp [15] | CXS Trapezoids | CXS Rectangles | CXS Error |
|----------------|------------------------|------------------------|------------------------|------------------------|-----------|
| Axial | 3.551×10^7 | 3.794×10^7 | 3.551×10^7 | 3.778×10^7 | 0.0% |
| Flap Bending | 2.088×10^9 | 2.178×10^9 | 2.088×10^9 | 2.161×10^9 | 0.0% |
| Lag Bending | 1.108×10^{10} | 9.100×10^9 | 1.108×10^{10} | 1.292×10^{10} | 0.0% |
| Torsion | 2.006×10^9 | 1.696×10^9 | 1.951×10^9 | 2.070×10^9 | 2.7% |
| Ext-Bend | -3.381×10^8 | -3.238×10^8 | -3.381×10^8 | -3.821×10^8 | 0.0% |
| Mass | 1.841×10^{-7} | 1.960×10^{-7} | 1.843×10^{-7} | 1.960×10^{-7} | 0.1% |
| I1 | 6.826×10^{-5} | - | 6.831×10^{-5} | 7.828×10^{-5} | 0.1% |
| I2 | 1.082×10^{-5} | 1.125×10^{-5} | 1.083×10^{-5} | 1.121×10^{-5} | 0.1% |
| I3 | 5.743×10^{-5} | 4.702×10^{-5} | 5.747×10^{-5} | 6.707×10^{-5} | 0.0% |
| Tension Center | 9.521 | 10.000 | 9.521 | 10.114 | 0.0% |

Table 2 –Isotropic blade-like section cross sectional properties.

Inspecting Table 2 the same behavior as the previous example is observed. The following comments can be made: i) the accuracy of CXS trapezoids is excellent, ii) the CXS rectangles overestimate the parameters due to duplication of the segment intersection, iii) the CXS rectangles and PreComp give very similar results, iv) the lag stiffness and inertia results of PreComp do not show the classical overestimation; it is suspected that a modeling error is present in the results presented in [15], v) PreComp is not very consistent, some variables are over-predicted and others are under-predicted, vi) again, the CXS trapezoids are more flexible than VABS only in torsion. The latter is expected since the present formulation neglects hoop moments [18]. The CXS geometric reconstruction of the blade-like section with trapezoidal elements can be seen in Figure 8.

417
418

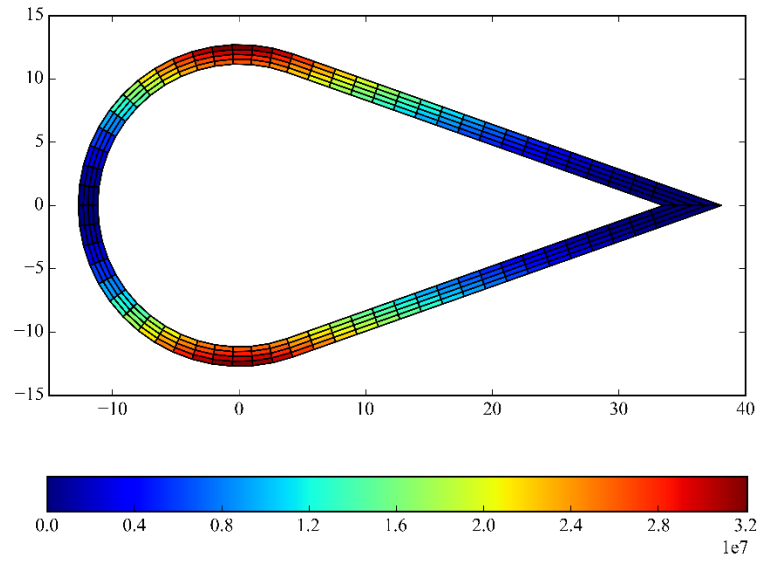


Figure 8 – Bending stiffness density colormap of the blade-like section.

419
420
421
422

423 5.3 Anisotropic oval pipe

424 This example consist on a multi-layer composite pipe with oval shape [12], see Figure 4. The
425 pipe is thick-walled and anisotropic; the lamination stacking sequence is unsymmetrical and
426 unbalanced.

427 Besides VABS results, the PreComp data presented in [15] will be used to benchmark the
428 present formulation. It must be noted that in [15], dimensioning of the inner and middle
429 radiuses of the oval is incorrectly reported; the total thickness of the cross section is 5.08 mm
430 instead of 2.54 mm. Also the material properties were wrongly informed, the constants used in
431 the calculations are: $E_{11}=141.963$ GPa, $E_{22}=E_{33}=9.79056$ GPa, $G_{12}=G_{13}=G_{23}=5.9984$ GPa.

432
433

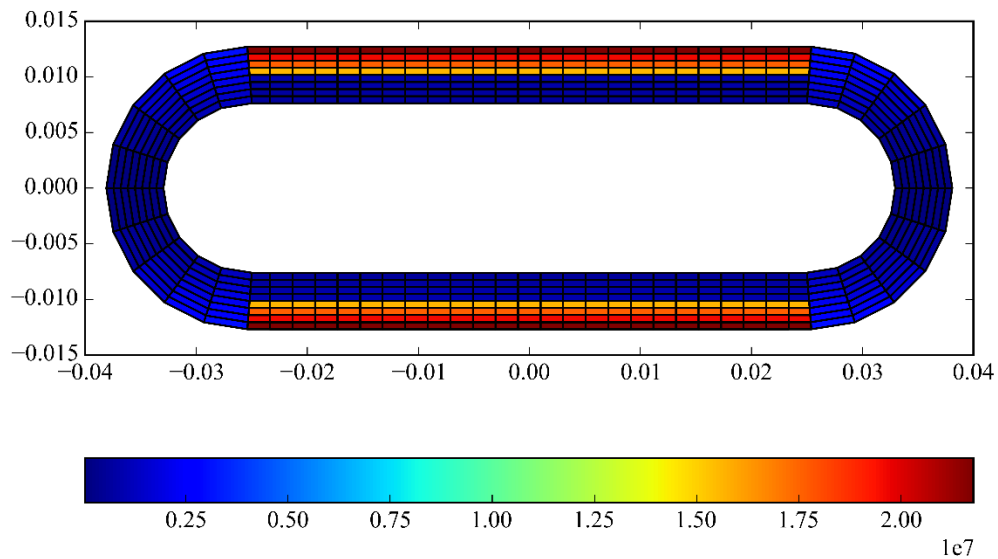


Figure 9 – Bending stiffness density of the anisotropic oval pipe.

434
435

This is a very unfavorable section for the present formulation because the lamination sequence is unbalanced and circumferentially asymmetric, then the errors that arise from the neglect of the circumferential curvature are maximized.

| | VABS | PreComp | CXS Trapezoids | CXS Rectangles | Error CXS Trapezoids | Error CXS Rectangles |
|------------|------------------------|-------------------------|------------------------|-------------------------|-------------------------|-------------------------|
| Axial | 4.606×10^7 | 7.833×10^7 | 4.580×10^7 | 4.760×10^7 | 0.5% | 3.3% |
| Bending 1 | 5.378×10^3 | 7.074×10^7 | 5.355×10^3 | 5.444×10^3 | 0.4% | 1.2% |
| Bending 2 | 1.532×10^4 | 4.857×10^4 | 1.530×10^4 | 1.704×10^4 | 0.1% | 11% |
| Torsion | 1.959×10^3 | 8.628×10^3 | 1.722×10^3 | 2.132×10^3 | 12% | 8.8% |
| Ext-Bend 2 | 2.088 | - | 1.856 | -3.028×10^{-1} | 11% | 12% |
| Ext-Bend 1 | -4.117 | - | -3.856 | -1.314 | 6% | 6% |
| Ext-Tors | 1.079×10^4 | -1.205×10^{-2} | 1.258×10^4 | 4.420×10^3 | 16% | 16.5% |
| Mass | 8.957×10^1 | - | 8.957×10^1 | 8.830×10^1 | 0.0% | 0.0% |
| I1 | 5.499×10^{-4} | - | 5.498×10^{-4} | 5.599×10^{-4} | 0.0% | 0.0% |
| I2 | 7.661×10^{-5} | - | 7.660×10^{-5} | 8.046×10^{-5} | 0.0% | 0.0% |
| I3 | 4.733×10^{-4} | - | 4.732×10^{-4} | | 0.0% | |

Table 3 – Anisotropic oval pipe cross sectional properties.

Despite this the Table 3 shows that the trapezoidal element still has a very good performance; for the most critical terms, the extensional-bending and the extensional-torsional couplings, the results are acceptable.

The maximum error (16%) is that of the extensional-torsional coupling; this far below the error reported in [15] for other one dimensional codes. There, the best results are given by is Pre-Comp, predicting an extensional torsional coupling of -1.2×10^{-2} . This represents an error of six orders of magnitude.

Again, the CXS rectangle element is not as accurate as the trapezoid; although, the results are consistent; both CXS elements give better results than PreComp.

From the observation of the torsional values an important remark can be made. Compared to VABS, the trapezoidal element predicts a lower torsional stiffness (12% error) while the rectangular element predicts a higher stiffness (8.8% error). Although at first glance it could be said that the rectangular element has a better performance, this is not so. The prediction of the torsional stiffness of a CAS laminated cross section done by an algorithm without significant geometrical errors should be below the real value; this is because the zero hoop moment assumption flexibilizes the cross section [18]. This flexibilization is also present in the rectangular element; however, the rectangular element overestimates the areas and thus overcompensates the flexibilization caused by the zero hoop moment assumption. Therefore, it is very important to note that although the torsional stiffness error is lower in the rectangular element, the prediction is worse.

5.4 The MH104 wind turbine blade [15]

In this example a real wind turbine cross section is analyzed; the cross section is presented in [15]. Geometrical and material data details can be found in the mentioned reference. To facilitate the VABS modeling, both the Gelcoat and the Nexus layers were removed from the model. This affects slightly the mass and inertia constants, but otherwise the VABS model would be very difficult to generate. The Figure 10 shows the geometry of the MH104 blade reconstructed by CXS.

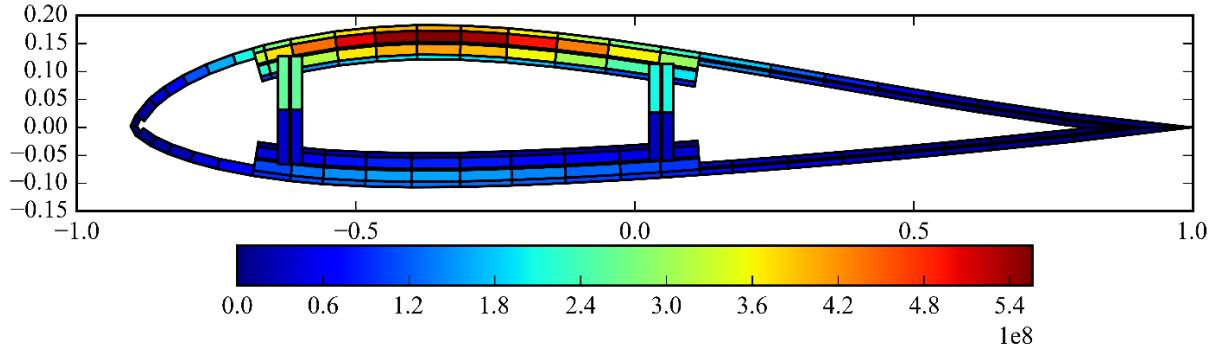


Figure 10 – Bending stiffness density of the MH104 wind turbine blade.

The stiffness and mass results are presented in Table 4.; again, it can be seen that the trapezoids give a better prediction than the rectangles. The following comments can be made: i) the axial, flap and lag stiffness is overpredicted by both CXS elements, ii) the torsional stiffness is underpredicted by both CXS elements; this is due to disregarding hoop moments iii) the torsional stiffness error of the rectangular element is smaller than that the trapezoidal element; this is caused by the stiffening caused by the duplication of areas of the rectangle element, iv) all coupling terms are very well predicted, v) the mass and inertia parameters predicted by the trapezoidal elements agree very closely to that of VABS.

| | VABS | CXS Trapezoids | CXS Rectangles | Error Trapezoids | Error Rectangles |
|----------|----------------------|----------------------|----------------------|---------------------|---------------------|
| Axial | 2.443×10^9 | 2.547×10^9 | 2.616×10^9 | 4.2% | 7.1% |
| Flap | 2.164×10^7 | 2.301×10^7 | 2.330×10^7 | 6.3% | 7.6% |
| Lag | 4.683×10^8 | 4.887×10^8 | 5.338×10^8 | 4.3% | 13.9% |
| Torsion | 2.693×10^7 | 2.24×10^7 | 2.344×10^7 | -16.8% | -12.9% |
| Ext-Flap | 7.006×10^7 | 7.263×10^7 | 7.411×10^7 | 3.6% | 5.7% |
| Ext-Lag | -4.695×10^8 | -4.900×10^8 | -4.631×10^8 | 4.3% | -1.3% |
| Ext-Tors | -3.293×10^7 | -2.986×10^7 | -2.937×10^7 | -9.3% | -10.8% |
| Mass | 2.601×10^2 | 2.603×10^2 | 2.693×10^2 | 0.0% | 3.5% |
| I1 | 5.620×10^1 | 5.619×10^1 | 6.255×10^1 | -0.0% | 11.2% |
| I2 | 5.381×10^1 | 5.380×10^1 | 6.013×10^1 | -0.0% | 11.7% |
| I3 | 2.381 | 2.385 | 2.415 | 0.1% | 1.4% |

Table 4 – MH104 blade cross sectional properties.

Observing the results presented in [15] and [12] and comparing them with the present results it can be seen that they are very sensitive to modeling details. In order to alleviate this issue the above calculations were generated with exactly the same geometrical data.

5.5 Sandia SNL100-3 Blade

Sandia National Laboratories have been working intensively in the design of a 100 meter wind turbine blade [30, 31]; up to date, this is the largest blade design in the world. The last design, named SNL100-3, incorporates carbon fiber and flat-back airfoils to the original all-glass blade. In this example the results of the blade stiffness and mass parameters at the maximum chord station of the Sandia SNL100-3 blade are presented. The blade geometry reconstructed with CXS is shown in Figure 11.

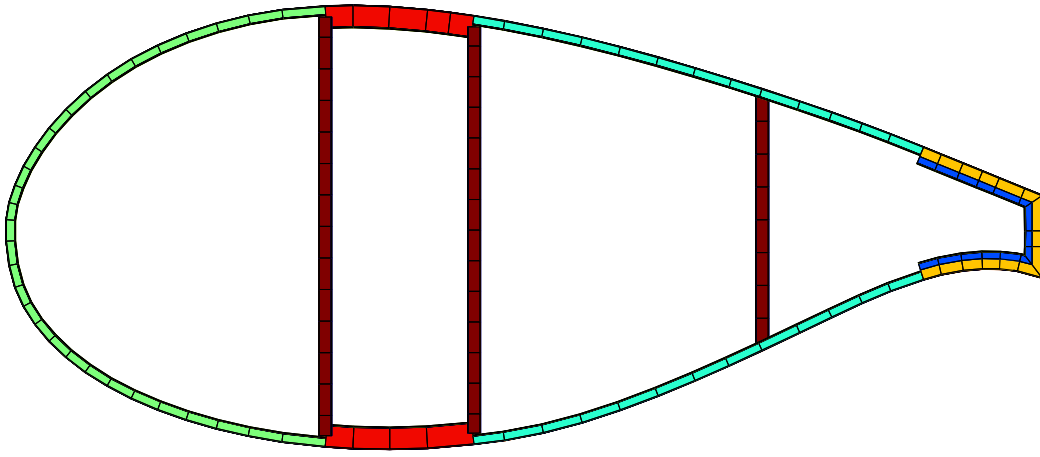


Figure 11 – Geometrical reconstruction of the station 18 of the SNL100-8 blade.

As before, the benchmark is done taking the VABS results as baseline. Both the VABS and the CXS models were generated using the geometric and material data published by Sandia [31]. Also, the Pre-Comp results are taken from the cited Sandia report.

| | VABS | Pre-Comp [31] | CXS Rectangles | CXS Trapezoids | Error (%) | | |
|--------------|------------------------|------------------------|------------------------|------------------------|-----------|-----------|-----------|
| | | | | | PreComp | CXS Rect. | CXS Trap. |
| Axial | 2.349×10^{10} | 2.425×10^{10} | 2.427×10^{10} | 2.375×10^{10} | 3.2 | 3.3 | 1.1 |
| Flap | 2.109×10^{10} | 2.193×10^{10} | 2.160×10^{10} | 2.128×10^{10} | 4.0 | 2.4 | 0.9 |
| Lag | 3.685×10^{10} | 3.390×10^{10} | 3.951×10^{10} | 3.700×10^{10} | -8.0 | 7.2 | 0.4 |
| Torsion | 1.526×10^{10} | 1.342×10^9 | 1.551×10^9 | 1.507×10^9 | -12.1 | 1.6 | -1.2 |
| Mass | 6.534×10^2 | 6.803×10^2 | 6.793×10^2 | 6.627×10^2 | 4.1 | 4.0 | 1.4 |
| Flap Inertia | 3.708×10^2 | 3.908×10^2 | 3.823×10^2 | 3.789×10^2 | 5.4 | 3.1 | 2.2 |
| Lag Inertia | 2.118×10^3 | 1.617×10^3 | 2.269×10^3 | 2.127×10^3 | -23.7 | 7.1 | 0.4 |
| X_{tc} | 0.473 | 0.485 | 0.488 | 0.468 | 2.5 | 3.2 | -1.1 |

Table 5 – Sandia SNL100-3 blade cross sectional properties.

From the results presented in Table 5 the following comments can be made: i) as usually, the CXS trapezoids give better results than CXS rectangles and PreComp, ii) CXS is consistent in the sense that it overpredicts the stiffness and mass parameters, except for the torsional stiffness. The torsional stiffness is, as expected, underpredicted; this is because the formulation neglects the hoop moments, iii) PreComp is not consistent, parameters are overpredicted or underpredicted randomly.

As a closing remark, it is noted that VABS computing time was 309 seconds while CXS computing time was 0.1 second. Besides, generation of the VABS model took approximately 6 hours, while the CXS model took 20 minutes.

6 CONCLUSIONS

The presented approach has proven to be very effective in computing the cross sectional stiffness and inertia properties of realistic composite blades. Different benchmark tests were performed and a detailed comparison of several inertia and stiffness terms was done. It was shown that the simplest version of the classical lamination theory can yield accurate results if the cross section is properly modeled.

The structural requirements of modern wind turbine blades are such that both discontinuous thickness distribution and reinforcement via shear webs is unavoidable. As a consequence, the geometric reconstruction of the cross section from the aerodynamic profile of the blade is not a trivial task. The proposed algorithm can reconstruct the full blade as a group

of rectangles or trapezoids using solely a thickness distribution table and a discretized version of the blade aerodynamic profile.

Two types of segments, unmatching rectangles and unmatching trapezoids, have been implemented in an algorithm called CXS. The unmatching trapezoid has shown an excellent performance, being very accurate and algorithmically stable. This element can reconstruct effectively extremely thick-walled sections as well as sections with discontinuous thickness distributions.

All stiffness and mass matrices have shown an excellent agreement with VABS, including the coupling stiffness terms and the tension centers. The torsional stiffness terms are the most inaccurate, the maximum error found for the torsional stiffness was 12%.

The numerical results show that provided the cross section is geometrically well represented, the proposed LLA can give results very close to a good SLA without losing any of the very well-known advantages of LLAs; i.e.: reduced modeling and execution times and algorithmic flexibility.

7 ACKNOWLEDGEMENTS

The authors wish to acknowledge the supports from Grupo de Investigación en Multifísica Aplicada at Universidad Tecnológica Nacional, CONICET and FONCYT. The authors also wish to thank Prof. Wenbin Yu for providing VABS.

REFERENCES

- [1] Saravia CM. A large deformation–small strain formulation for the mechanics of geometrically exact thin-walled composite beams. *Thin-Walled Structures*. 2014;84:443-51.
- [2] Hu T. A validation and comparison about VABS-IDE and VABS-GUI. All Graduate Plan B and other Reports. Paper 334. <http://digitalcommons.usu.edu/gradreports/334>; Utah State University; 2012.
- [3] Hau E. *Wind Turbines*. 2nd ed. Berlin: Springer; 2006.
- [4] Zhu T, Ertekin E. Resolving anomalous strain effects on two-dimensional phonon flows: The cases of graphene, boron nitride, and planar superlattices. *Physical Review B*. 2015;91:205429.
- [5] Zhu T, Ertekin E. Phonon transport on two-dimensional graphene/boron nitride superlattices. *Physical Review B*. 2014;90:195209.
- [6] UpWind. Design limits and solutions for very large wind turbines. <http://www.upwind.eu/2011>. p. 108.
- [7] Spera DA. *Wind Turbine Technology*. New York: ASME; 2009.
- [8] Jonkman JM, Butterfield S, Musial W, Scott G. Definition of a 5-MW Reference Wind Turbine for Offshore System Development. National Renewable Energy Laboratory; 2009.
- [9] Hansen MOL. *Aerodynamics of Wind Turbines*. London: Earthscan Publications Ltd.; 2008.
- [10] Hansen MOL, Sørensen JN, Voutsinas S, Sørensen N, Madsen HA. State of the art in wind turbine aerodynamics and aeroelasticity. *Progress in Aerospace Sciences*. 2006;42:285-330.
- [11] Laird DL. *NuMAD User's Manual*. Sandia National Laboratories; 2001.
- [12] Saravia MC, Saravia LJ, Cortínez VH. A one dimensional discrete approach for the determination of the cross sectional properties of composite rotor blades. *Renewable Energy*. 2015;80:713-23.
- [13] Boulanger P, Hayes M. Extended Polar Decompositions for Plane Strain. *J Elasticity*. 2006;83:29-64.
- [14] Cesnik CES, Hodges DH. VABS: A New Concept for Composite Rotor Blade Cross-Sectional Modeling. *Journal of the American Helicopter Society*. 1997;42:27-38.
- [15] Chen H, Yu W, Capellaro M. A critical assessment of computer tools for calculating composite wind turbine blade properties. *Wind Energy*. 2010;13:497-516.

567 [16] Hodges DH, Yu W. A rigorous, engineer-friendly approach for modelling realistic, composite
568 rotor blades. *Wind Energy*. 2007;10:179-93.

569 [17] Saravia CM, Machado SP, Cortínez VH. A composite beam finite element for multibody
570 dynamics: Application to large wind turbine modeling. *Engineering Structures*. 2013;56:1164-76.

571 [18] Hodges DH. *Nonlinear Composite Beam Theory*. Virginia: American Institute of Aeronautics
572 and Astronautics, Inc.; 2006.

573 [19] Yu W, Volovoi VV, Hodges DH, Hong X. Validation of the variational asymptotic beam
574 sectional analysis. *IAA Journal*. 2002;40:2105-13.

575 [20] Philippidis TP, Vassilopoulos AP, Katopis KP, Voutsinas SG. A software for fatigue design and
576 analysis of composite rotor blades. . *Wind Engineering*. 1996;20:349-62.

577 [21] Bir G. User's Guide to PreComp.
578 <http://wind.nrel.gov/designcodes/preprocessors/precomp/PreComp.pdf>; National Renewable Energy
579 Laboratory; 2005.

580 [22] Lindenburg C. STABLAD. Stability analysis tool for anisotropic rotor blade panels. Energy
581 Research Center of the Netherlands; 2008.

582 [23] Resor B, Paquette J, Laird DL, Griffith DT. An evaluation of wind turbine blade cross section
583 analysis techniques. 18th Structural Dynamics and Materials Conference. Orlando, Florida:
584 American Institute of Aeronautics and Astronautics; 2010.

585 [24] Malcolm DJ, Laird DL. Extraction of equivalent beam properties from blade models. *Wind*
586 *Energy*. 2007;10:135-57.

587 [25] Resor B, Paquette J. Uncertainties in prediction of wind turbine blade flutter. *Structural*
588 *Dynamics and Materials Conference*. Denver, Colorado: American Institute of Aeronautics and
589 Astronautics; 2011.

590 [26] Saravia MC. A large deformation-small strain formulation for the mechanics of geometrically
591 exact thin walled beams *Thin-Walled Structures*. 2014;In Press.

592 [27] Barbero E. *Introduction to Composite Material Design*. London: Taylor and Francis; 2008.

593 [28] Librescu L. *Thin-Walled Composite Beams*. Dordrecht: Springer; 2006.

594 [29] Crisfield MA. *Non-Linear Finite Element Analysis of Solids and Structures: Advanced Topics*:
595 John Wiley & Sons, Inc.; 1997.

596 [30] Griffith DT, Ashwill TD. The Sandia 100-meter all-glass baseline wind turbine blade: SNL100-
597 00. Sandia National Laboratories; 2011.

598 [31] Griffith DT, Richards PW. The SNL100-03 Blade: Design Studies with Flatback Airfoils for the
599 Sandia 100-meter Blade. Sandia National Laboratories; 2014.